ACCESS
Arctic Climate Change
Economy and Society

Project no. 265863

ACCESS

Arctic Climate Change, Economy and Society

Instrument: Collaborative Project
Thematic Priority: Ocean.2010-1 "Quantification of climate change impacts on economic sectors in the Arctic"

D1.23 – Report on analysed data from IMBs

Due date of deliverable: **31/12/2013**
Actual submission date: **05/02/2014**

Start date of project: **March 1st, 2011** Duration: **48 months**

Organisation name of lead contractor for this deliverable: **SAMS**

Project co-funded by the European Commission within the Seventh Framework Programme (2007-2013)		
Dissemination Level		
PU	Public	X
PP	Restricted to other programme participants (including the Commission Services)	
RE	Restricted to a group specified by the consortium (including the Commission Services)	
CO	Confidential, only for members of the consortium (including the Commission Services)	

Contents

1. Introduction

Sea Ice Mass Balance buoy (SIMBA) buoy is designed and manufactured in Scottish Association for Marine Science (SAMS). It consists of a GPS receiver, an Iridium receiver/transmitter, a series of individually addressable temperature sensors and heaters at 2 cm intervals along a 5-m chain (and 50 cm intervals along a 5-m chain within water column), and a battery power supply. The chains are deployed through 2-inch auger holes, extending completely through the ice and into the water column, with a segment suspended vertically above the air/snow interface. The temperature sensors are normally sampled four times a day, have a temperature resolution of 0.06°C, and were calibrated prior to deployment. Once the chain being deployed, each heater/sensor pair is used to detect the phase of the medium in which the sensor is sitting, through periodically heating and recording the relaxation of the temperature signal to the pre-heating value. For the detailed technical description please refer to Jackson et al (2013).

In ACCESS project, through collaboration with Korea Polar Research Institute (KOPRI) and SATICE project, we deployed total of 14 SIMBAs during 2011 and 2012 summers in the Arctic. Primary objective of the SIMBA deployment is to study small-scale (within climate model grid size) thermodynamic and dynamic processes of sea ice and their interactions with the upper ocean properties. The 2011 deployment was made in the northern Chukchi Sea, while the 2012 deployment was made close to the East Siberian Sea.

In this report we describe deployment and environmental conditions in Section 2. Detailed analysis of SIMBA data is presented in Section 3, in which we describe the results based on the deployment year. For 2011 SIMBA data our analysis highlights differential ice bottom melt rate observed from SIMBAs and the effects of solar radiative warming. As you see in this report the differential melt rate is closely related to heterogeneous distribution of solar heating (dominantly through the variation of sea ice concentrations) within a spatial scale of 90 km. For 2012 SIMBA data analysis we highlight the role of inertial ice motion in association with fluctuation of warm and cold water temperature in the upper-ocean mixed layer as well as detection of the interface between ice bottom and underlying water from SIMBAs. We also report small-scale floe deformation events that observed from 2012 SIMBA data.

2. SIMBA deployment

2.1. 2011 SIMBA deployment

On 7-8 August 2011, total of six SIMBAs were deployed in the Chukchi Borderland Region (CBL, around 77° 44′N and 162° 18′W) (see Figure 2.1 for the location). The deployment was made through collaboration with 2011 KOPRI R/V *Araon* Arctic research expedition. The detailed information of the 2011 SIMBA deployment is listed in Table 2.1. Figure 2.1 shows the GPS tracks of six SIMBAs from the deployment (August 2011). While some SIMBAs failed to send the data, Access09 (blue line) survived and transmitted GPS data until May 2, 2012 (Table 2.1). As shown in Figure 2.1, all SIMBAs were deployed within 15 km, but they were diverged around and mainly drifted to the east following the Beaufort Gyre.

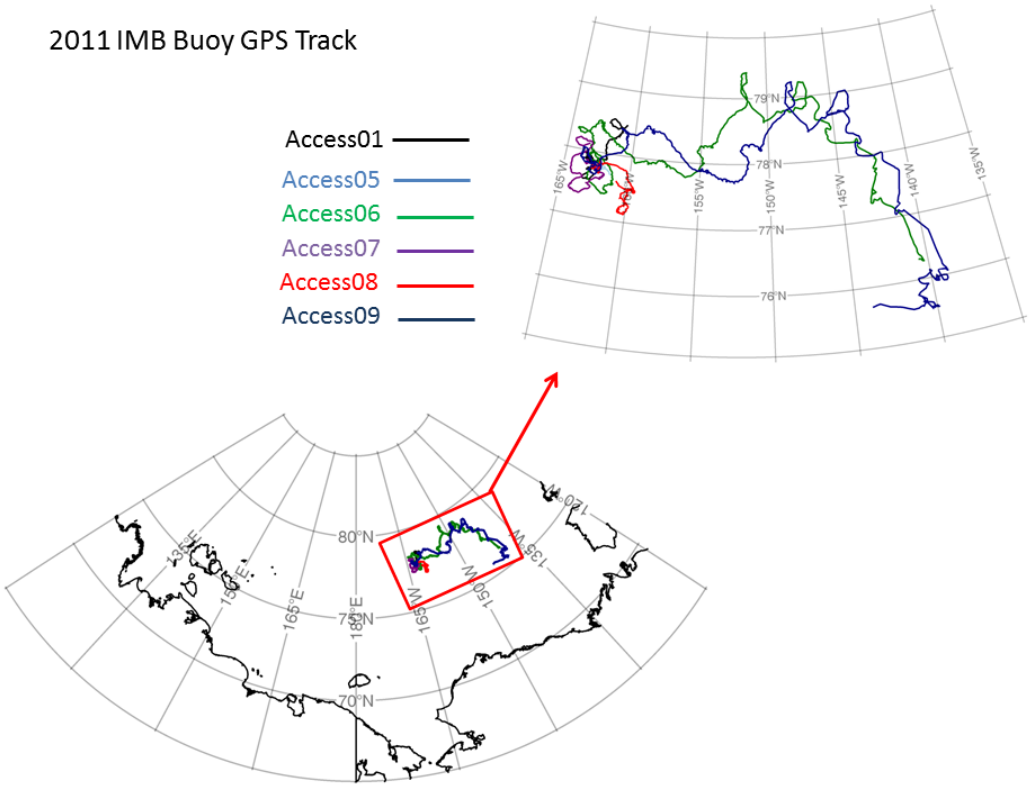

Figure.1 GPS tracks of SIMBAs deployed during 2011 summer.

Sea ice condition at the deployment site and surrounding area can be seen from the TerraSAR-X Synthetic Aperture Radar (SAR) image taken 6 hours before the deployment as well as photograph taken during the deployment (Figure 2.2). Floe #1 (where *Araon* was moored to) is shown in darker tone ice floe of about 2 km wide. There was open water area in the south of Floe #1 which was widening throughout the deployment period. The ice floes in the area were characterised by large coverage of melt ponds (Figure 2.2). SIMBAs were deployed on Floe #1 and in surrounding area (Table 2.1). At Floe #1 we deployed Access01 right beside high-precision GPS buoy (SATICE) as shown in Figure 2.3. The remaining five

SIMBAs were deployed within 15 km from the Floe #1 through the helicopter on board *Araon* (see Figure 2.3). All SIMBAs were deployed on multiyear ice (MYI) (including second-year ice). The floe size was around one or two hundred meters except Floe #1 (Access01) and #2 (Access07).

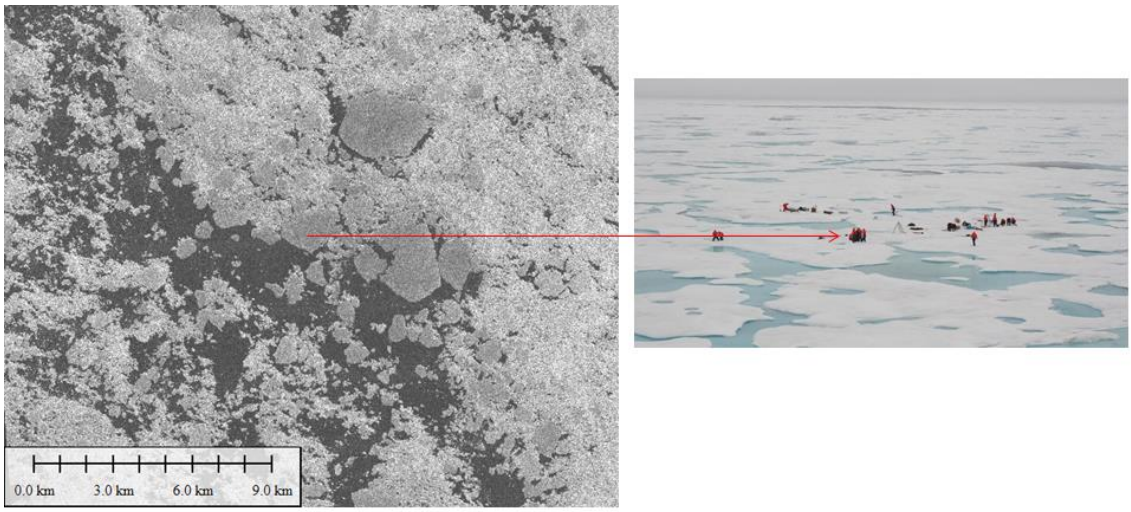

Figure.2 TerraSAR ScanSAR (©DLR) image taken on August 6 at 17:48 UTC, 9 hours prior to the deployment. The photograph at the right shows large coverage of melt ponds on Floe #1.

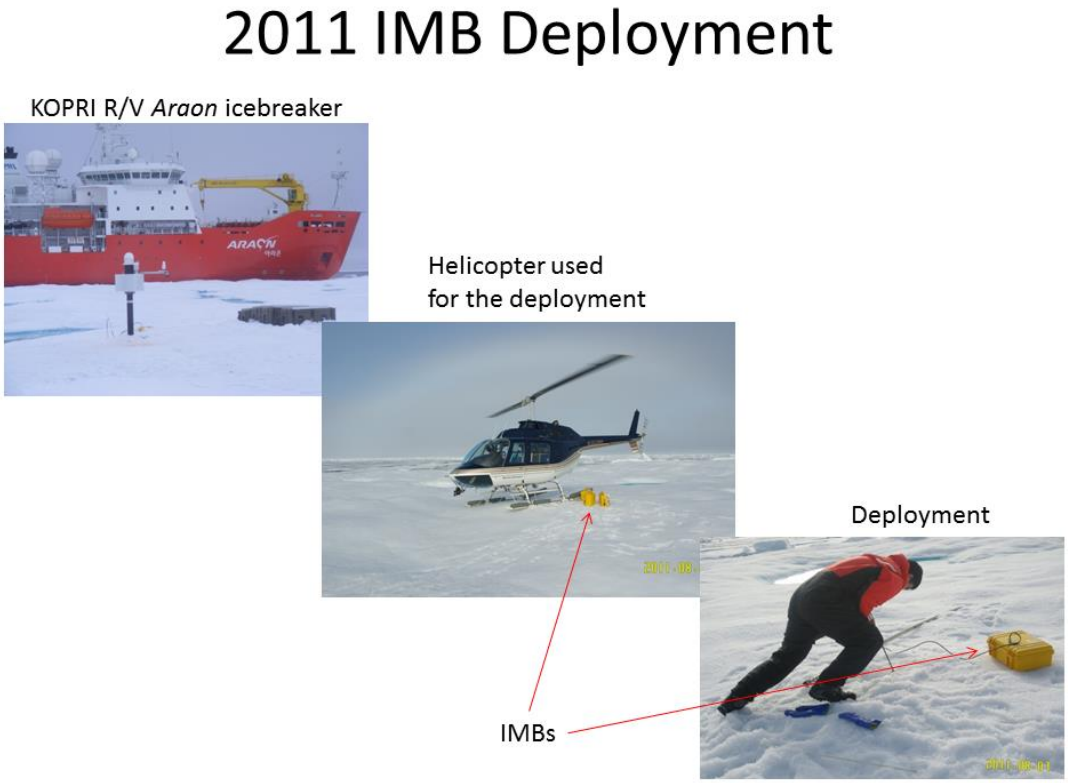

Figure.3 Photographs taken during SIMBA deployment. Photographs courtesy to A. Masanov (AARI) and P. Elosegui (CSIC).

Table.1 Summary of 2011 SIMBA deployment.

Buoy ID	Deployment Data	GPS Data	T-chain Data	Comments
Access 1	07/08/2011 04:09 UTC N77˚44.792' W162˚18.492' Ice thick: 2.60 m Freeboard; 52 cm Snow depth: 8 cm Sensor at the ice surface: 13/14	2011.08.07 04:54 UTC -> 2011.09.10 18:54 UTC	2011.08.07 05:54 -> 2011.09.10 21:54 UTC	Deployed on Floe #1. Sensor spacing=2cm. # of temp sensors=132 # of td sensors = 192 Temp sensor below #133 didn't send via Iridium due to errors.
Access 5	07/08/2011 20:21 UTC N77 46.488' W161 53.326' Ice thick: 2.90 m Freeboard: 30 cm Snow depth: 7 cm Sensor at the ice surface: 12/13	2011.08.07 20:54 UTC -> 2011.08.17 14:00 UTC	2011.08.07 23:54 -> 2011.08.17 15:54 UTC	Deployed 5 nm East of Floe #1. Sensor spacing=2cm. # of temp sensors=132 # of td sensors = 192 Temp sensor below #133 didn't send via Iridium due to errors.
Access 6	07/08/2011 19:51 UTC N77 51.826' W162 15.900' Ice thick: 3.74 m Freeboard: n/a cm Snow depth: 4 cm Sensor at the ice surface: 13/14	2011.08.07 19:00 UTC -> 2012.01.22 09:54 UTC	2011.08.07 22:54 -> 2012.08.25 23:10 UTC	Deployed 5 nm North of Floe #1. # of temp sensors=132 # of td sensors = 239 Temp sensor below #133 didn't send via Iridium due to errors.
Access 7	07/08/2011 00:43 UTC N77 47.745' W162 5.484' Ice thick: 2.96 m Freeboard: 31 cm Snow depth: 5 cm Sensor at the ice surface: 18	2011.08.07 00:46 UTC -> 2011.09.10 12:43 UTC	2011.08.07 04:43 -> 2011.09.10 14:44 UTC	Deployed on Floe #2 (with SATICE02). Sensor spacing=2cm. # of temp sensors=132 # of td sensors = 239 Temp sensor below #133 didn't send via Iridium due to errors.
Access 8	07/08/2011 20:50 UTC N77 41.269' W162 13.826' Ice thick: 2.24 m Freeboard: 48 cm Snow depth: 8 cm Sensor at the ice surface: 18	2011.08.07 21:46 UTC -> 2011.09.03 06:53 UTC	2011.08.07 22:43 UTC -> 2011.09.03 02:46 UTC	Deployed 5 nm South of Floe #1. Sensor spacing=2cm. # of temp sensors=132 # of td sensors = 239 Temp sensor below #133 didn't send via Iridium due to errors.
Access 9	08/08/2011 01:43 UTC N77 48.067' W162 12.268' Ice thick: 3.50 m (4.00* corrected based on data) Freeboard: 50 cm Snow depth: n/a Sensor at the ice surface: 19	2011.08.08 03:22 UTC -> 2012.05.02 09:47 UTC	2011.08.08 10:22 UTC -> 2011.10.19 04:24 UTC 2011.10.19 16:26 UTC chain broken (default numbers only)	Deployed 5 nm West of Floe #1 (with SATICE01). Sensor spacing=2cm. # of temp sensors=240 # of td sensors = 239

2.2. 2012 SIMBA deployment

The 2012 ACCESS SIMBA deployment was made in collaboration with 2012 KOPRI *Araon* Arctic expedition and SATICE project. The expedition originally planned to cover the region between the northern Chukchi Sea and the border of East Siberian Sea, but substantial ice loss in the region prompted the cruise to divert northward in search of suitable ice and adequate sea ice concentration (SIC) for buoy deployment. Guided by passive-microwave SIC maps and helicopter reconnaissance surveys, a deployment region was selected in the region bordering the East Siberian Sea and the northern Chukchi Sea (81° 40.38 ″N and 174° 15.56 ″E; Figure 2.4a). The SIC at the time of deployment was more than 70% and comprised a melange of ice floes of various sizes (from tens of meters to tens of kilometres). Larger ice floes mostly consisted of first-year ice (FYI) pans embedded with smaller pieces of MYI that could be recognized by its higher freeboard, undulating topography, and the presence of blue-like melt ponds on its surface.

Total of eight SIMBAs were deployed. All 2012 SIMBAs were prefixed with “KOPRI” to distinguish them from 2011 SIMBAs. In Figure 2.4 we use abbreviated prefix “KP” to denote 2012 SIMBA and the prefix “SI” stands for SATICE buoy (high-precision GPS buoys deployed along with SIMBAs). The “2010I” in Figure 2.4 indicates the seasonal sea ice mass balance buoy (SIMB), deployed behalf of CRREL (U.S. Army Cold Regions Research and Engineering Laboratory). As all SIMBAs deployed on the single ice floe, the GPS tracks are shown in single line (Figure 2.5). The ice floe drifted predominantly to the south-east until March 2013, and then shifted the direction to north-east. The longest surviving buoy was KP08 that has been transmitting GPS data until December 11, 2013.

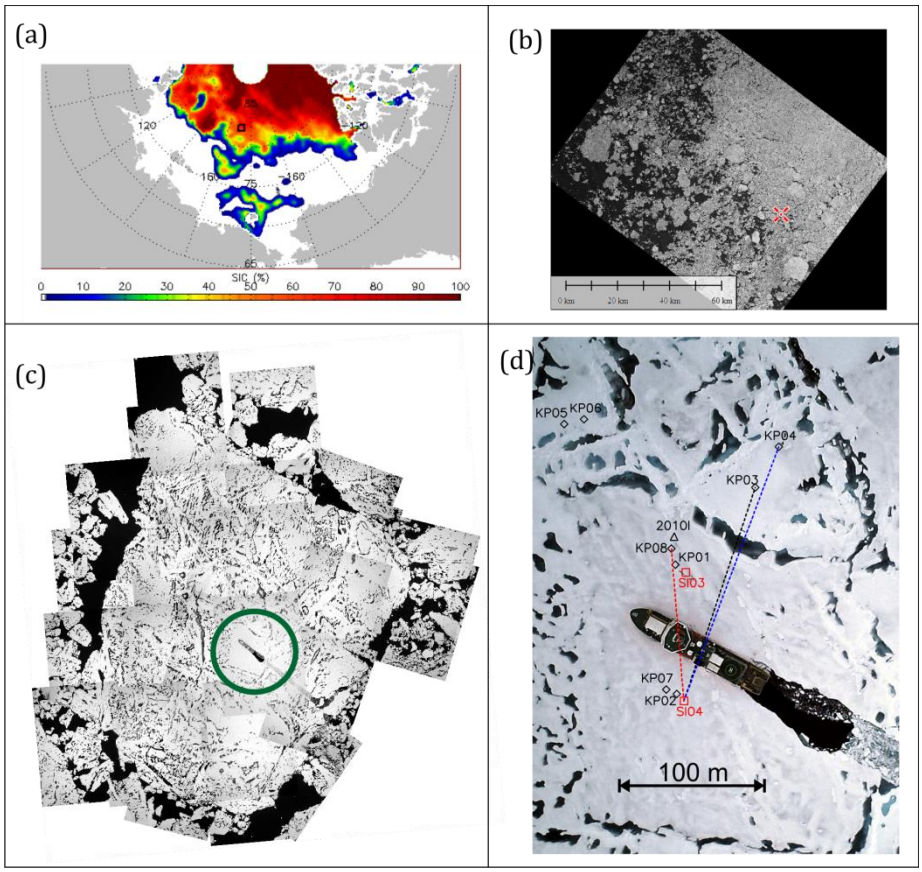

FigureErreur ! Il n'y a pas de texte répondant à ce style dans ce document.**.4 (a) Sea ice concentration during the buoy deployment, on 14 August 2012, with deployment location marked as a black rectangular box. (b) TerraSAR-X ScanSAR image (©DLR) acquired on August 29 (15 days after deployment) with floe location marked as a red diagonal crosshair symbol. (c) Aerial mosaic from photos taken on August 14 but rotated to match the orientation of the floe on August 15 06:00 UTC. The green circle marks the location of IBRV *Arao*n, which is about 100-m long. (d) Zoom in with buoy locations overlaid on the aerial mosaic. In the photo black, blue, and red dashed lines depict baselines to SI04 from KP03, KP04, and KP08, respectively. In all panels, North (East) is direction is to the top (right).**

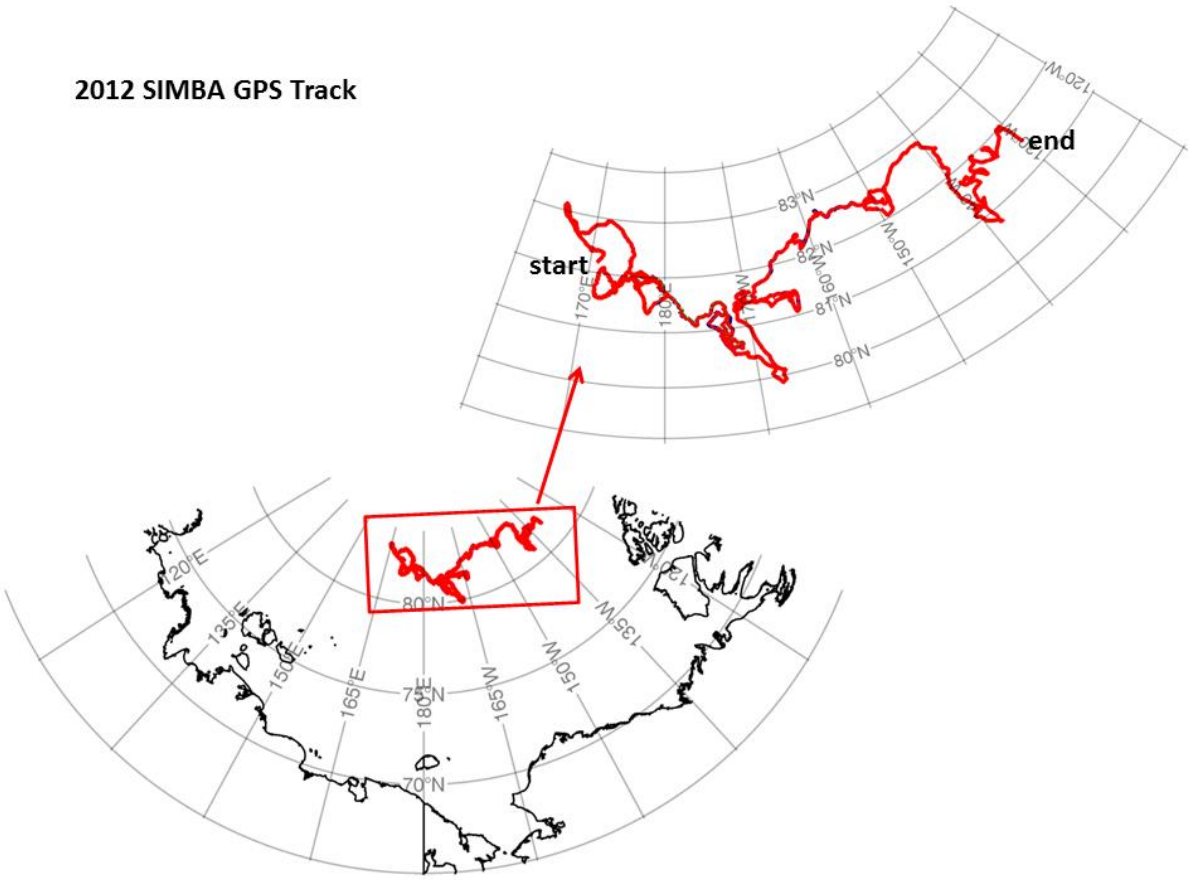

Figure.5 GPS tracks of 2012 SIMBAs.

Table. 2 Summary of 2012 SIMBA data.

Buoy ID	Deployment Data	GPS Data	T-chain Data (last operation date)	Comments
KOPRI 01	13/08/2012 23 UTC Ice thick: 1.28 m Freeboard;7.5 cm Snow depth: 10 cm Sensor at the top: 1 Sensor at snow suf: 14 Sensor at the ice surf: 19/20 Sensor at the freeboard: 24/25	2012.08.14 00:19 UTC -> 2012.09.14 22:00 UTC	2012.09.14 23:01 UTC (temp) 2012.09.14 17:06 UTC (td1) 2012.09.14 17:08 UTC (td2)	Deployed on the level FYI about 6 m from SI03. Prematurely failed.
KOPRI 02	14/08/2012 20 UTC Ice thick: 1.06 m Freeboard; 8 cm Snow depth: 11 cm Sensor at the top: 1 Sensor at snow suf: 14 Sensor at the ice surf: 21/22 Sensor at the freeboard: 25/26	2012.08.15 00:06 UTC -> 2013.07.16 14:23 UTC	2012.12.31 17:09 UTC (temp) 2012.12.28 17:49 UTC (td1) 2012.12.28 17:50 UTC (td2)	Deployed on the level FYI about 6 m from SI04. Temp show strange values from 28/12/2012, and T-chain stop working from 28/12/2012. But GPS continued to work until 16/07/2013!
KOPRI 03	15/08/2012 03 UTC Ice thick: 3.17 m Freeboard; 37 cm Snow depth: 14 cm Sensor at the top: 1 Sensor at snow suf: n/a Sensor at the ice surf: 21/22 Sensor at the freeboard: 39/40	2012.08.15 05:19 UTC -> 2013.05.08 18:19 UTC	2012.12.21 17:09 UTC (temp) 2012.12.19 05:15 UTC (td1) 2012.12.19 05:15 UTC(td2)	Deployed on the MYI about 100 m from the starboard side of the ship. T-Chain stop working from 19-21 Dec, but GPS continued to work.
KOPRI 04	15/08/2012 03 UTC Ice thick: 1.08 m Freeboard; n/a Snow depth: n/a Sensor at the top: 1 Sensor at snow suf: n/a Sensor at the ice surf: 32/33	2012.08.15 04:00 UTC -> 2013.07.06 19:10 UTC	2012.08.27 12:00 UTC (temp) 2012.08.27 12:05 UTC (td1) 2012.08.27 12:05 UTC (td2)	Deployed on the MYI about 150 m from the ship's starboard side. T-Chain prematurely failed, but GPS continued to work.

	Sensor at the freeboard: 32/33			
KOPRI 05	15/08/2012 05 UTC Ice thick: 3.00 m Freeboard; 30 cm Snow depth: 5 cm Sensor at the top: 1 Sensor at snow suf: n/a Sensor at the ice surf: 23/24 Sensor at the freeboard: 38/39	2012.08.15 05:07 UTC -> 2012.12.11 16:07 UTC	2012.12.21 16:07 UTC (temp) 2012.12.19 16:11 UTC (td1) 2012.12.19 16:11 UTC (td2)	Deployed on the MYI about 150 m from the ship's bow
KOPRI 06	15/08/2012 05 UTC Ice thick: 1.43 m Freeboard; 24 cm Snow depth: 15 cm Sensor at the top: 1 Sensor at snow suf: n/a Sensor at the ice surf: 20/21 Sensor at the freeboard: 32/33	2012.08.15 07:00 UTC -> 2012.08.23 20:00 UTC	2012.12.21 15:32 UTC (temp) 2012.12.19 15:36 UTC (td1) 2012.12.19 15:37 UTC (td2)	Deployed on the same MYI with KP04. GPS prematurely failed. Ice thick adjusted to 1.50m in the quick plots (to match with ice bottom from the plots).
KOPRI 07	14/08/2012 20 UTC Ice thick: 1.01 m Freeboard; 0.5 cm Snow depth: 12 cm Sensor at the top: 1 Sensor at snow suf: 21 Sensor at the ice surf: 27 Sensor at the freeboard: 28	2012.08.14 23:00 UTC -> 2012.12.14 19:11 UTC	2012.12.19 11:00 UTC (temp) 2012.12.19 07:14 UTC (td1) 2012.12.19 07:15 UTC (td2)	Deployed on the smooth FYI about 10 m from SI04.
KOPRI 08	13/08/2012 23 UTC Ice thick: 1.07 m Freeboard; 1 cm Snow depth: 9.2 cm Sensor at the top: 1 Sensor at snow suf: 19 Sensor at the ice surf: 22/23 Sensor at the freeboard: 23/24	2012.08.14 00:00 UTC -> 2013.12.11 19:33 UTC	2012.12.21 08:24 (temp): T-chain below ice 2012.12.20 09:15 (td1/2): T-chain below ice	Deployed on the smooth FYI about 20 m from SI03. 2012.12.21 08:24 (temp): T-chain below ice stop working, but upper part of T-chain sending the data until 2013.06.15 (but doesn't know about the quality of the data is good or not)

3. Analysis of SIMBA data

3.1. Analysis of 2011 SIMBA data

3.1.1. Selection of two SIMBA buoys

In this analysis we focused on the two selected SIMBAs (Access08 and 09) as they provide the full data suite necessary for the present analysis. In this section we call Access08 and Access09 as SIMBA08 and SIMBA09 for the convenience. These two buoys (s/n 08 and 09) were deployed on MY ice floes which were 3.50 to 3.74 meter thick and about 200 meter wide (Table 2.1). Immediately after deployment on 8 August, SIMBA08 (marked in red in Figure 3.1) was located just about 8-km south of SIMBA09 (marked in blue in Figure 3.1). The two ice floes then began to drift differentially, and were separated by about 90 km by the end of August. While SIMBA08 last successfully fully transmitted data until September 3, SIMBA09 continued to function until October 23. The mean ice drift speed for SIMBA08 was about 0.16 m s^{-1} (ca. 13.7 km day^{-1}) over the common drift duration from the deployment to August 31, while the mean speed for SIMBA09 was about 0.15 m s^{-1} (ca. 12.9 km day^{-1}) for the same period. Position is known with accuracy of standard GPS which is about 5 to 10 m. The drift tracks of two buoys show a sequence of semi-diurnal loops, typical of inertial motion at the 12.3 hour inertial period for this latitude (Figure 3.1). At the time of deployment, sea ice concentration was about 70-80% in the vicinity of both buoys (Figure 3.1d), of which about 15-30% was MY ice (visual observation). The thickness of first-year ice was estimated at 0.7 m or less (visual observations), whilst the MY ice varied from 3 to 5 m thick based on ten different drill-hole measurement within 5-km from the deployment site.

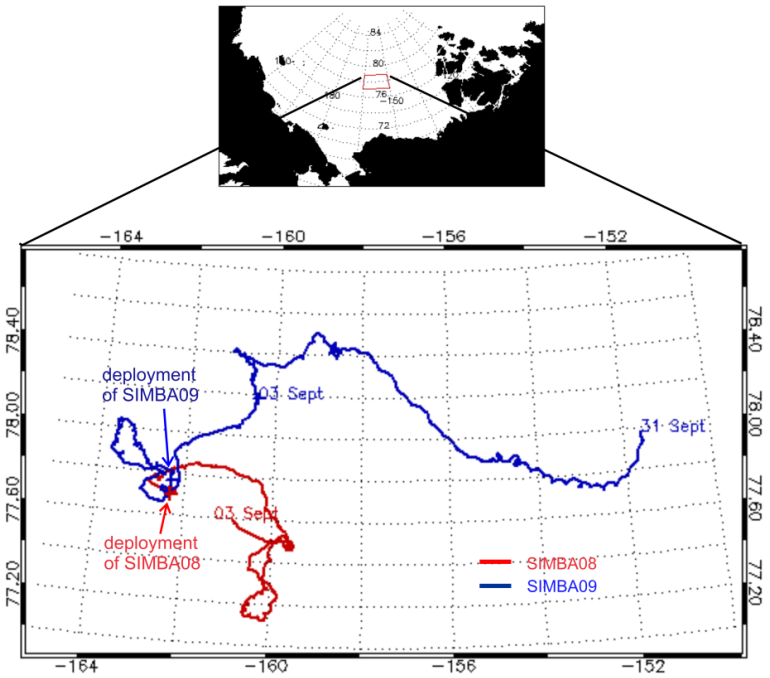

FigureErreur ! Il n'y a pas de texte répondant à ce style dans ce document.**.6 Map of GPS tracks of two SIMBAs from August 8 to September 31. Location of two buoys at the deployment is marked as plus symbol, and the dates shown in the figure are the location of the buoys on that dates. The study area is shown as red box in the small insert in the figure.**

3.1.2. Estimation of bottom ice melt

Inference of ice growth or melt at the bottom of sea ice depends on accurate localization of the ice-water interface, which in the case of SIMBA buoys relies on measurement of both the ambient temperature (T) and the thermal response of the immediate surroundings of the heater/sensor pairs to short periods of heating, i.e. the temperature elevation (δT_h) above ambient. Through controlled experiments in an ice tank, three criteria were found to contribute to determination of the phase of the medium surrounding the sensors: (1) for water temperatures significantly higher than the ice temperature a sharp temperature gradient occurs at the ice-water interface, (2) temporal variability in both T and δT_h is often greater in the water column than within ice due to variable ice-ocean relative motion, and (3) a local maximum in δT_h occurs at the ice-water interface. Accuracy in determining the depth of the interface (h) is set by the 2 cm spacing of heater/sensor pairs. The rate of change in the position of the interface along the chain ($-dh/dt$) is interpreted as the bottom melt rate.

Bottom melt rates from SIMBA08 and 09 were similar and increased with time for the period prior to 17 August, after when they diverged, with the melt rate at SIMBA08 increasing to a maximum of more than 5 cm day^{-1} and the rate for SIMBA09 reduced to 2 cm day^{-1} (Figure 3.2a). During the period between 17 and 28 August, the air temperatures at the buoys were similar, but both sea ice concentration (SIC) and water temperature (T_w) diverged, with SIC decreasing earlier and T_w increasing earlier for SIMBA08 than for SIMBA09 (Figure 3.2b-d). The trends of the changing SIC and T_w suggest that the sharp decrease in SIC in the vicinity of SIMBA08 after 17 August contributed to the enhancement of solar heating of the near-surface ocean and thus increased bottom ice melt rate (Figure 3.2).

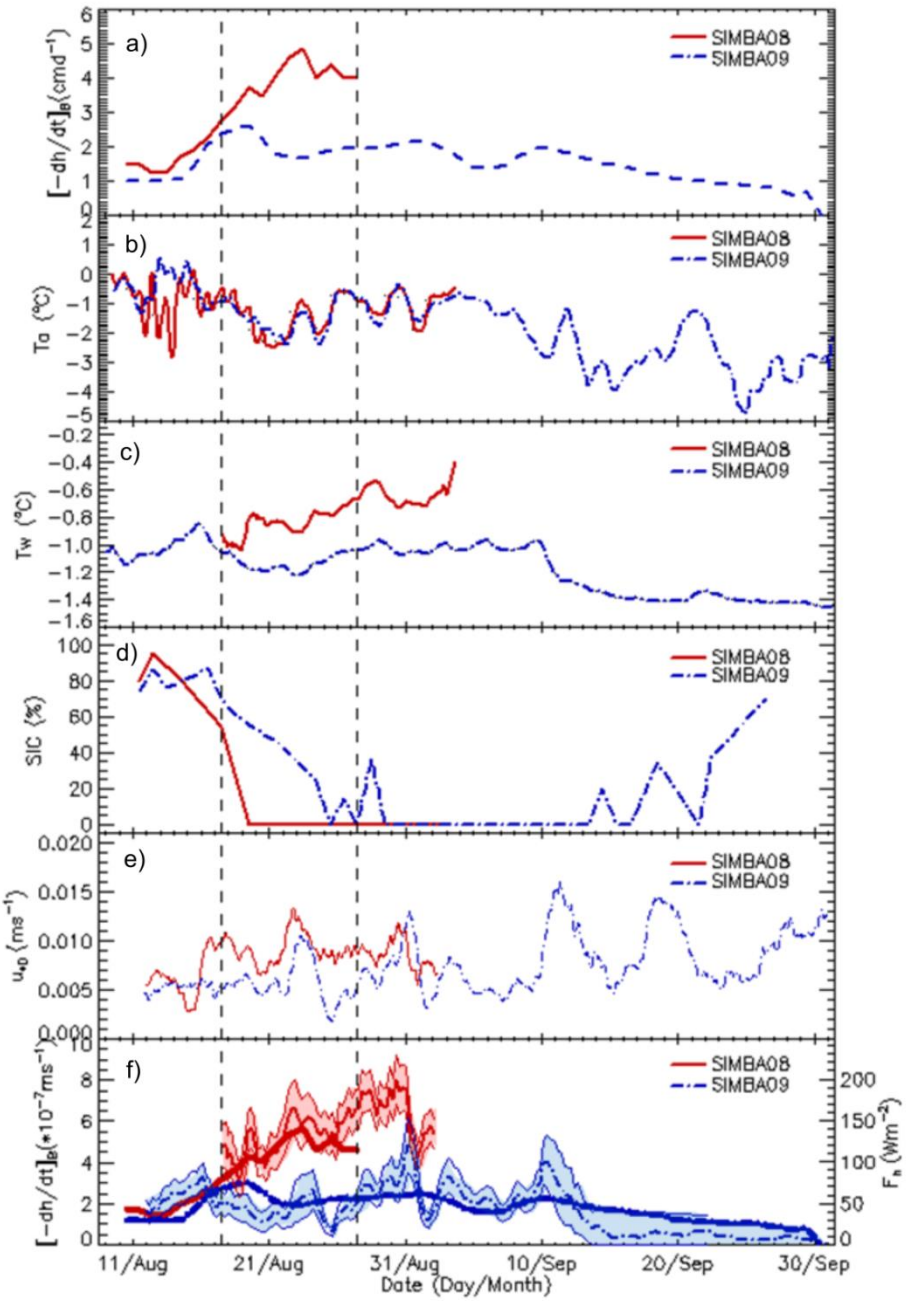

Figure.7 Temporal variation of (a) observed bottom ice melt rate (-dh/dt), (b) air temperature (T_a), (c) water temperature (T_w), (d) sea ice concentration (SIC), (e) friction velocity (u_{*0}), and (f) estimated ocean-to-ice heat flux (F_h) and bottom melt rate $(-dh/dt)_{Fh}$ at SIMBA08 and 09 sites. Observed melt rates were 5-day moving-averaged. T_a is one-day moving average of the vertical mean over 10 sensors at 20 to 40 cm above the snow. T_w is one-day moving average of the vertical mean over the bottom 5 (19) sensors for SIMBA08 (SIMBA09). T_w at SIMBA08 before August 17 is not available due to a communication problem. Heat fluxes and melt rates shown in (f) use freezing temperature T_f based on S = 26 psu (solid line) and S = 28 psu and 24 psu for upper and lower bounds, respectively. The thick lines are the observed values, also shown in (a). The two vertical dashed lines mark the dates of August 17 and 27. The ice temperature at the two sites ranged -1.2 to -1.3°C.

3.1.3. Estimation of ocean-to-ice heat flux

The observed rate of change of ice thickness can be compared to the equivalent rate of ice loss through the ocean-to-ice heat flux. For this purpose we estimated the heat flux from a widely used parameterization based on analysis of under-ice deployments of turbulence clusters (McPhee, 1992),

$$F_h = \rho_w C_p C_h u_{*0} \delta T \quad (2.1)$$

where F_h varies with the friction velocity (u_{*0}) at the ice-water interface, and the temperature above freezing ($\delta T = T_w - T_f$), and in which ρ_w=1028 kg m^{-3} is the density of sea water, C_p=3980 J kg^{-1} is the specific heat of sea water, and C_h=0.0057 is a heat transfer coefficient (McPhee and others, 2003). Assuming the surface geostrophic current is negligible relative to the ice drift velocity, u_{*0} can be calculated using the Rossby similarity drag law (McPhee, 2008) with known ice drift velocity vector (***V***) as follows;

$$\frac{V}{u_{*0}} = \frac{1}{k}(\log(Ro_* - A - iB) \quad (2.2)$$

where κ=0.4 is von Karman's constant, A=1.91 and B=2.12 are the Rossby-similarity parameters (McPhee, 1979), $Ro_* = u_{*0}/(fz_0)$ is the surface friction Rossby number, f is the Coriolis parameter, and z_0=0.01 m is the surface roughness length (McPhee, 2003). The values of u_{*0} shown in Fig. 4e range from 0.002 to 0.016 m s^{-1}, and are comparable to those estimated for ice drift by Timmermans and others (2011). The temperature above freezing δT is calculated from the time series of buoy T_w and the mixed layer salinity value (Fofonoff and Millard, 1983). In our case observed salinity from ice-based CTD casts at the time of buoy deployment were S=26 psu, for which T_f= -1.414°C. The ocean-to-ice heat flux (F_h) and the equivalent bottom melt rate $(-dh/dt)_{Fh}$, for ice density of 900 kg m^{-3} and latent heat of fusion of sea ice of 2.76×10^5 J kg^{-1}, are shown in Figure 3.2f. Temporal and spatial variability in mixed layer salinity contributes to uncertainty in our estimates of T_f and thus F_h. The impact of salinity variability on the heat flux is incorporated into the estimates in Figure 2.5f through use of upper (S=28 psu, T_f= -1.526°C) and lower (S=24 psu, T_f= -1.303°C) bounds on the mixed layer salinity. At these levels of variability in mixed layer S, the estimated F_h values for SIMBA08 and 09 match well with the observations and are distinctively different.

3.1.4. Effects of solar heating

Between August 11 and 27, the net ice bottom melts along the SIMBA08 and 09 drift trajectories were 0.54 m and 0.26 m, respectively. We address here the question of whether local solar heating along these two trajectories can account for the difference between the heat inputs required to generate the observed ice melts for the SIMBA08 (162 MJ m^{-2}) and SIMBA09 (78 MJ m^{-2}) buoys. To investigate this, solar heat input to the ocean (F_{rw}) is estimated following Perovich and others (2008),

$$F_{rw} = F_r(1-\alpha)(1-SIC) \quad (2.3)$$

where F_r is incoming surface solar irradiance, *SIC* is sea ice concentration and α=0.07 is the albedo of open water. For sea ice concentration, we use the AMSR-E 12.5-km sea ice concentration product (AE_SI12) from NSIDC (Cavalierie and others, 2004). AE_SI12 has

shown the smallest mean error in comparison with other sea ice products (Meier, 2005) and is known to be less sensitive to melting summer ice (Markus and Dokken, 2002). For comparison, we computed the heat input (F_{rw}) using the incoming surface shortwave irradiation (F_r) from both NCEP-Department of Energy (DOE)'s Reanalysis 2 (NCEP2) and ERA-Interim (ERA-I) reanalysis data. F_r values from NCEP2 tend to be positively biased (up to 87 W m^{-2}) against Baseline Surface Radiation Network (BSRN) observations, whilst ERA-I F_r values tend to be only slightly negatively biased (-2.1 W m^{-2}) (Zib and others, 2012). The differences in F_r can be attributed to better resolution and an improved data assimilation scheme in ERA-I, which includes satellite data (Uppala and others, 2008). Independent evaluation of both NCEP2 and ERA-I daily F_r was carried out by comparing them with surface F_r measured on board *Araon* during August 2011 (Eppley PSP). Of Total 13 days compared, it showed that NCEP2 F_r overestimate by 63 W m^{-2} whilst ERA-I F_r underestimate by 20 W m^{-2}. Relative to the BSRN comparison, NCEP2 tends to slightly less overestimate F_r but ERA-I to more underestimate F_r. It however confirms the general trend found in the BSRN comparison.

Figure 3.3 shows the progression of spatial patterns of CF_{rw} using ERA-I F_r and the associated buoy tracks from August 11 onwards. Between August 8 and 15 the separation between the two buoys grew from about 8 km to about 70 km, as SIMBA08 drifted to the east while SIMBA09 drifted to the northwest (Figure 3.3a). Despite the differential drift, the differences in CF_{rw} experienced along the two buoy trajectories remain very small during this period (ca. 10 MJ m^{-2} for the buoy locations on 15 August, Figure 3.4). After August 17, the difference in CF_{rw} between the two buoy trajectories becomes much larger, reaching up to 60 MJ m^{-2} (137 MJ m^{-2}) for ERA-I (NCEP2) reanalysis data for the buoy positions on August 27 (Figure 3.4). This difference occurs as a result of differential ice motion as well as spatial and temporal heterogeneity in local solar radiative input. During this period, SIMBA08 drifted to an area in the south where much larger CF_{rw} occurred due to a sharp decrease in sea ice concentration in the area (Figure 3.4, and 3.3d). On the other hand SIMBA09 looped around the initial deployment site, where much smaller CF_{rw} resulted from a slower decrease in sea ice concentration (Figure 3.4 and 3.3d).

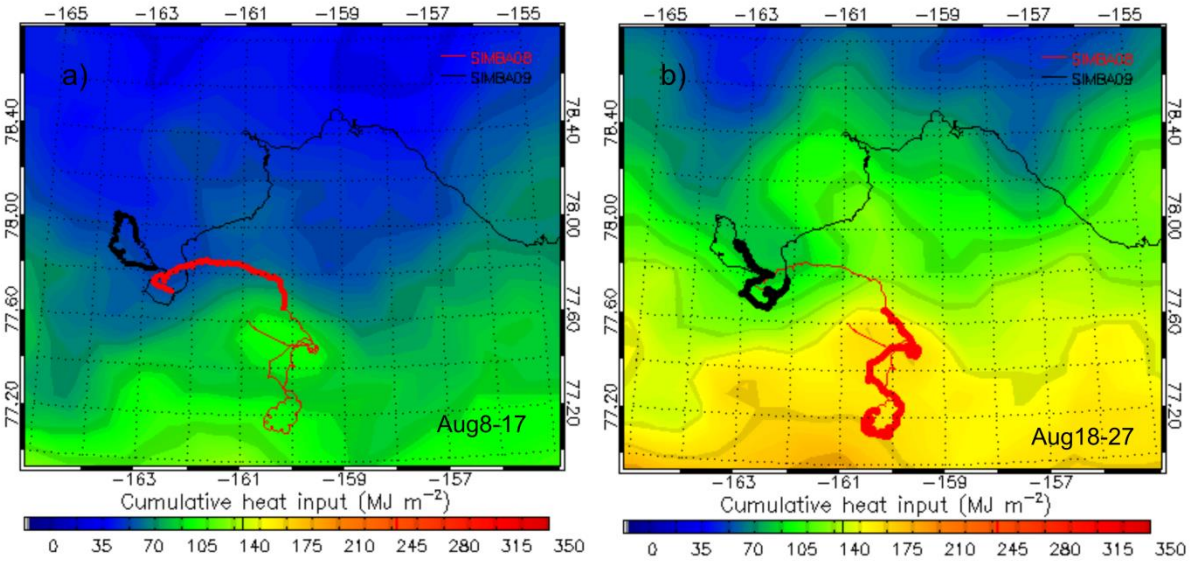

Figure.8 Map of solar heat inputs cumulated from January 1 until (a) August 17 and (b) August 27. Thin red and black lines are the GPS tracks of SIMBA08 and 09 between August 8 and September 31, respectively. Thick red and black lines are the GPS tracks of corresponding SIMBAs for the period shown in figures. Cumulative heat inputs (CF_{rw}) are calculated by integrating F_{rw} from Eq. 1 using ERA-I F_r values.

The heat required for the observed melt in late August lies between the NCEP2 and ERA-I bounds on solar heating, CF_{rw} (Figure 3.4). This suggests that the regional difference in local solar heating is a significant contributor to the observed difference in melt rates, if we regard the values shown for solar heat input using NCEP2 and ERA-I F_r as upper and lower estimates respectively. As discussed above, the overestimation of NCEP2 F_r has been found from both BSRN and our comparisons. Although ERA-I F_r is known to have a slight underestimation with BSRN observations (Zib and others, 2012), our independent evaluation shows the underestimation could be more severe. In addition a significant amount of solar energy can be transmitted to the upper ocean through melt-ponded ice cover (Ehn and others, 2011). Thus the parameterization in which no solar energy penetrates through the ice cover could underestimate the solar heating through ice cover as a whole.

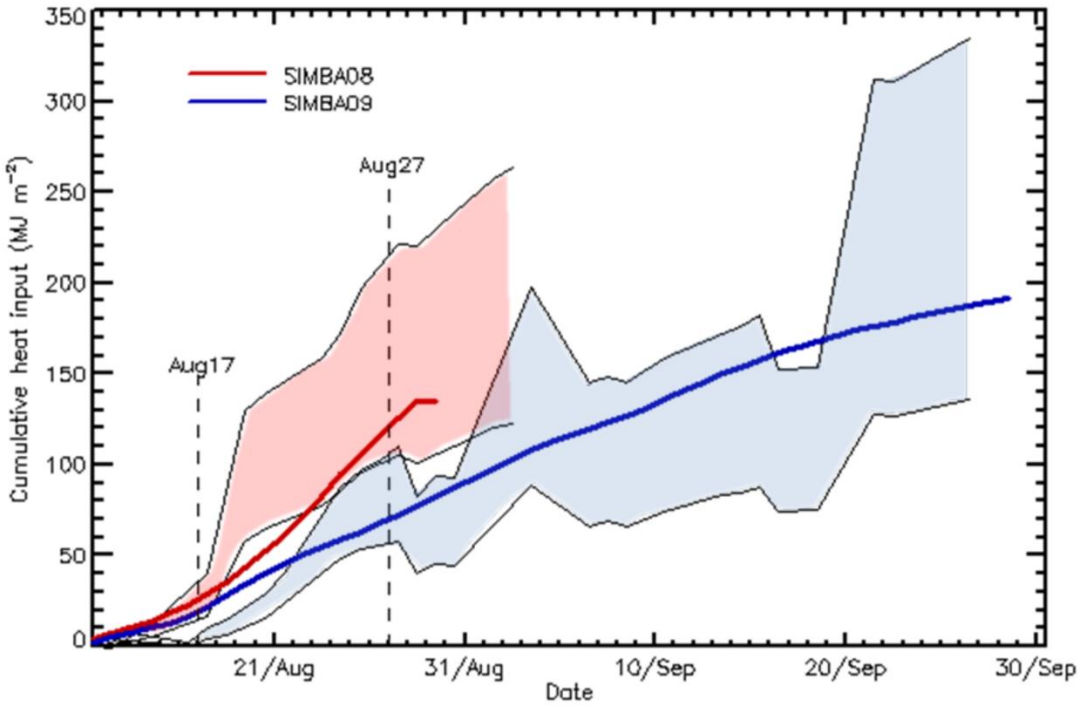

Figure.9 Temporal variations of cumulative solar heat inputs (CFrw) at the SIMBA08 (red) and 09 (blue) sites. The upper and lower borders of the shaded area are the values calculated by using the Fr values from NCEP2 and ERA-I data, respectively. Larger NCEP2 CFrw values are mainly due to larger Fr values in NCEP2 reanalysis data than in ERA-I (see text). The thick lines are the required heat input for the observed melt shown in figure 3.2a. The two dates at the top of vertical lines match with the dates of cumulative heat input maps shown in Fig 3.3.

3.2. Analysis of 2012 SIMBA data

3.2.1. Spatial and temporal variability of upper ocean temperature

The deployment of 2012 SIMBAs ("KP") was made near the boundary between northern Chukchi Sea and East Siberian Sea. In this region we found no trace of Pacific Summer Waters. In order to observe high temporal and spatial variability of upper-ocean mixed layer we set the temperature sampling rate of KP02 every 6 hours from August 16 to September 5, and then every one hour until September 17, and then reset to every three hours until October 25. At the same time the collaborative SATICE buoy measured the water temperature at every 10 min. As shown in Figure 3.5 these two temperature measurements show a good agreement each other. This suggests that temperatures observed at KP02 are reasonable compared to high precision CT sensor.

In Figure 3.5 we selected four warm water events. The first two events are very distinctive (over the duration of less than one day). The temperature rise was up to by about 0.2 °C (from -1.33 °C). This temperature rise is almost equivalent to increase in bottom ice melt rate by 2 cm day^{-1} (see Section 3.1 in this report), however these events are transient so that it is not clear how much they contribute actual bottom ice melt. Despite that the occurrence of warm water appears to be related to inertial motion of the ice floe, i.e., all four warm water events occur during distinctive inertial motion of the ice floe (Figure 3.5). Presence of warm

water mass within the mixed layer was also observed from 48-hour ice moored CTD data (personal communication, K. Shimada, 2012). The source of warm water mass is thought to be from radiative warming by solar radiation through patches of open water areas.

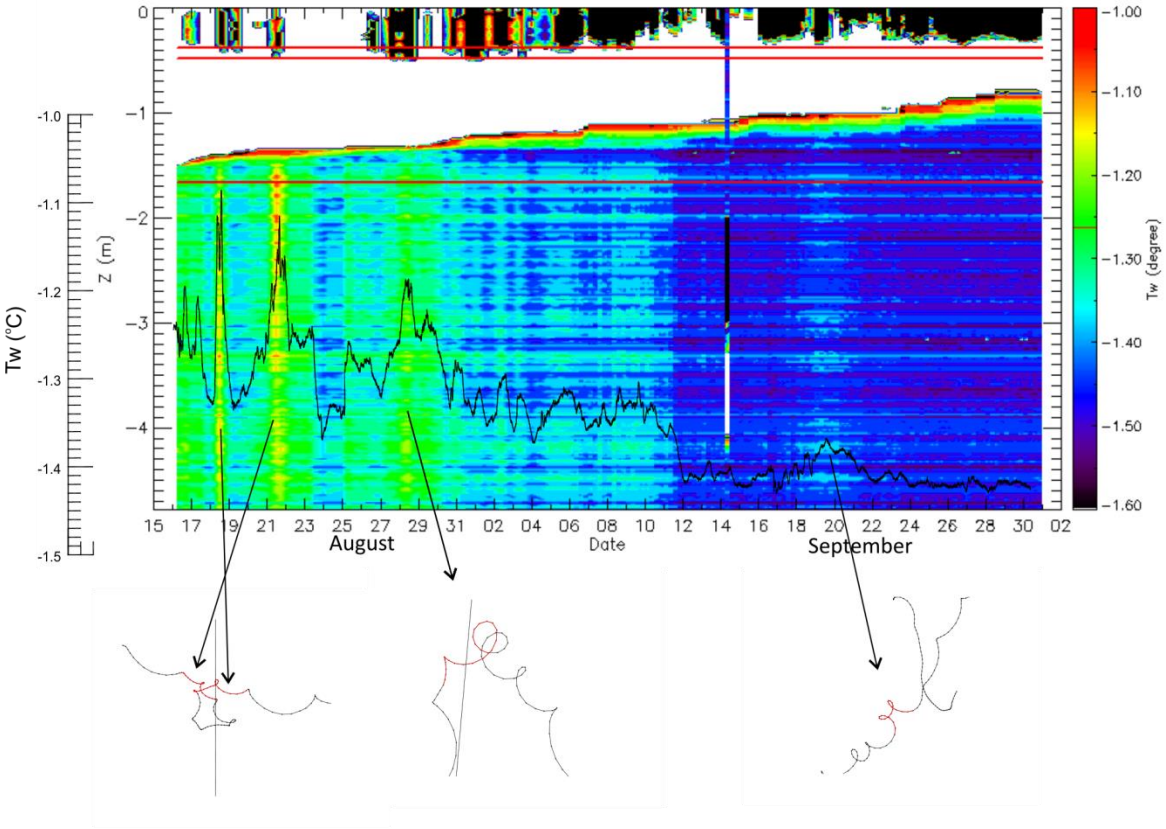

Figure.10 Temperature profile measured from KP02 (contour colour plot). The upper, middle and bottom red solid lines indicate the ice surface, freeboard and ice bottom measured at the deployment. Temperatures lower than -1.6 °C or higher than -1.0 °C were shown white or black colour. The water temperatures measured from SATICE CT sensor (black solid line) well agree with the temperature profile from KP02. At the bottom of the plot, it shows GPS trajectories during corresponding warm water events. Note that the white coloured area does not represent the ice, but rather cooling of ice from the bottom (see Section 3.2.2 for the details).

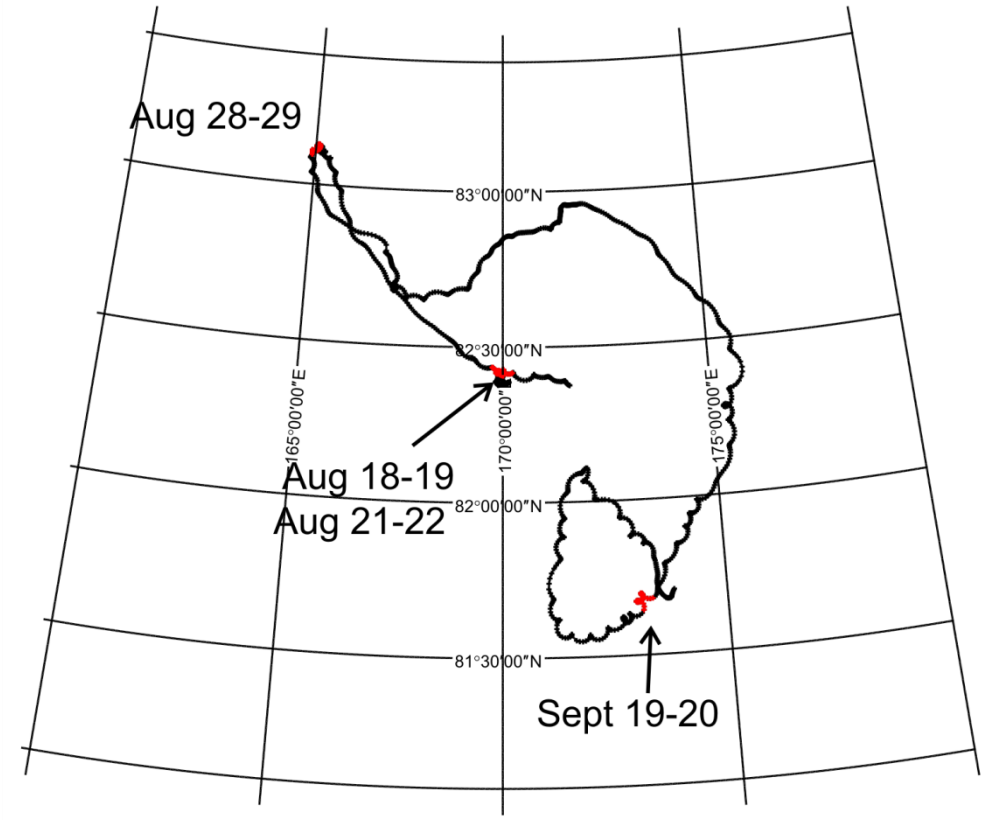

Figure.11 GPS locations of four warm water events. The first two events occur at the same region, and the third event (August 28-29) occurs at the tip of northwest corner of the track. Sea ice concentration (SIC) data shows that much less sea ice was occupied in the northwest part of the track, which indicates the third warm water event is associated with solar warming effects in that region as the ice floe drifted into there. However, the other three events occur randomly along the track.

3.2.2. Ice temperature, phase variation, and ice bottom detection

Example of ice temperature and temperature difference after the heating (TD) is shown in Figure 3.7. Here we show KP02 measurements to compare with the results in above section (Section 3.2.1). First note that temperature within ice interior went through warm to cold transition at the middle of October. Air temperature was below the freezing point since September, but the ice temperature remained warmer than the freezing point until mid-October. Cooling of ice temperature progressed from the ice bottom toward the ice surface (Figure 3.7a). It is important to note that the white-coloured region in Figure 3.5 does not represent ice. The interface between ice bottom and water can be more clearly seen from temperature difference (TD1 and TD2) plots (Figure 3.7b and c). The interface can be detected by looking at high TD values (red in the plots) as well as high temporal variation of TD in water column. This clearly demonstrates that temperature profile alone can produce erroneous results in ice bottom detection (so as to bottom melt and growth rates).

High temporal variation in TD values is associated with ice drift dynamics. When ice floe drifts fast, the heat generated by heating phase is quickly removed, and the TD becomes

smaller. On the other hand, when ice drifts slow the TD value increases in water column and also high TD value occurs at the ice bottom. Similar observation was made during independent laboratory experiment in the cold room at SAMS. This fluctuation in TD value is likely associated with inertial motion under free ice drift regime. This view is supported by the fact that this fluctuation in TD value stops around late October (Figure 3.7b and c). This coincided with the occurrence of cold air temperature (Figure 3.7a) which caused to the transition from free drift to consolidated ice (i.e. freeze-up, no more inertial motion).

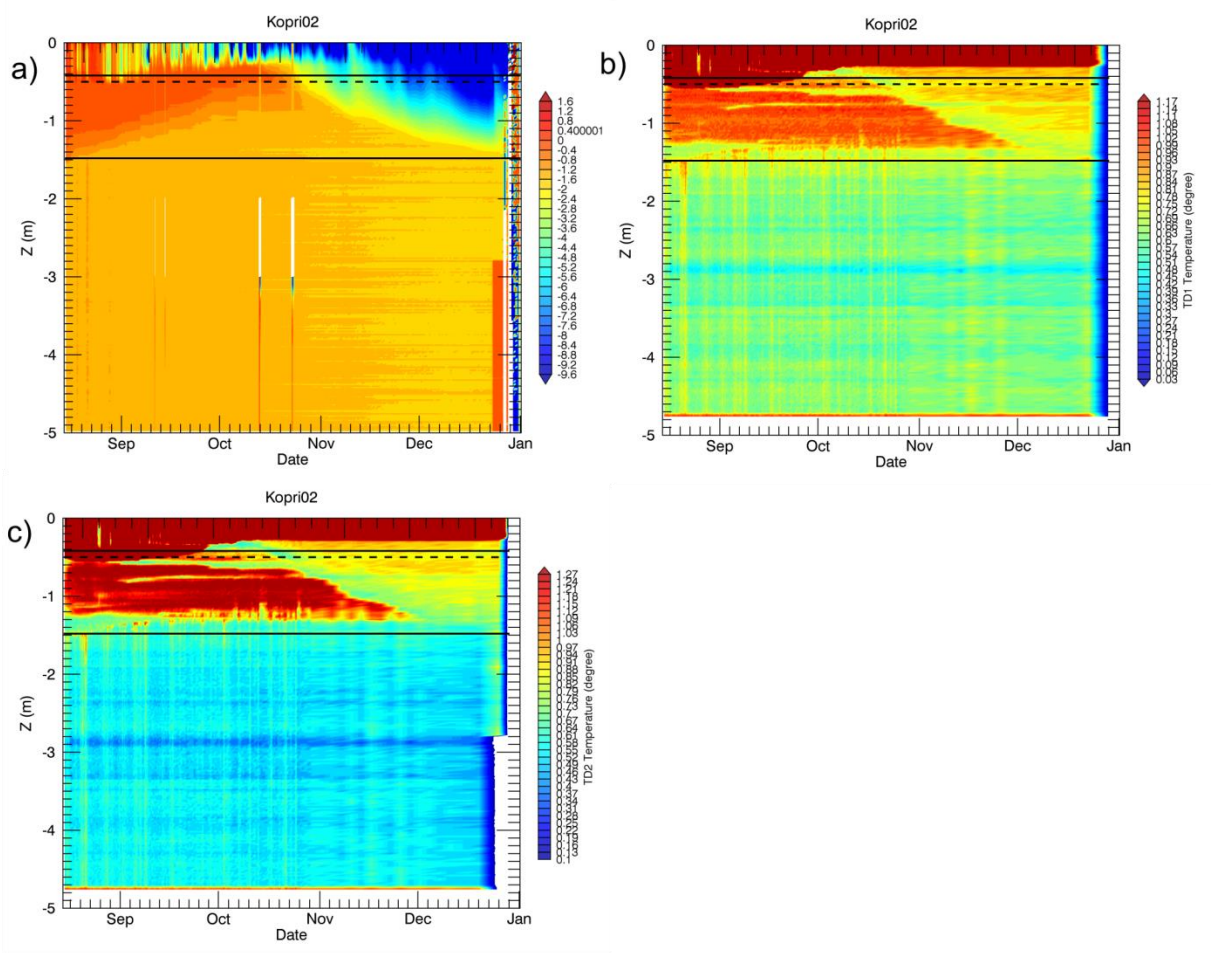

Figure.12 a) Ambient temperature (T), b) temperature difference after 30 sec (TD1) and c) after 99 sec (TD2) from Kopri02 (KP02) thermistor chain. The upper solid and dotted black lines are the ice surface and freeboard water level at the deployment of the buoy. The lower solid line is the interface between ice bottom and water.

3.2.3. Floe deformation

2012 SIMBA buoys were deployed on the single ice floe (but at various ice type/thickness) (see Section 2.2), which recorded unique floe deformation events. The eight ACCESS-KOPRI SIMBAs and two SATICE buoys were deployed within 200 m apart (see Figure 2.4d). Even though they were deployed within relatively small distance, high-precision GPS (cm-level precision) of SATICE (Elosegui et al. 2006) was paired with standard GPS measurement of SIMBAs, and this allows to measure changes in baseline distance and direction sufficient enough to detect small-scale deformation.

Between December 13 and December 22 the GPS data from these buoys reported the series of deformation events. Displacements of SIMBAs relative to one of SATICE buoy (SI04) are depicted in Figure 3.8 and details are shown in Table 3.1. The most dramatic deformation occurred during D21 (December 21 to 22). During this period the baseline distances were reduced by at least 50% (Table 3.1), which is shown as shrinking of buoy arrays in Figure 3.8c.

Consolidation of ice (i.e. freeze-up) commenced from mid-October based on ice drift dynamics (speeds, rotation) as well as series of TerraSAR ScanSAR imagery (©DLR) taken during that period. This means these deformation events occurred well after freeze-up. More detailed analysis of ice drift dynamics revealed a short period when the ice floe drifted freely during November 9 to 15. This can be clearly seen distinctive inertial loops in the GPS track (not shown here). This period coincided with the rise of atmospheric temperature up to almost 0 °C and strong wind stress (i.e. passing of a low pressure system). This suggests that the new ice start to form around existing floes was broken, allowing existing floes to drift freely but not causing deformation within the existing floe. Since then air temperature remained below -10 °C, which reconsolidated and thickened new ice around the existing floes. Deformations occurred about one month after the reconsolidation. This indicates the ice at the time of deformation was well consolidated and stiff enough to increase internal stress gradient upon strong wind stress.

Table.3 Baseline length L and orientation θ relative to SI04 of deformation events. ΔL and Δθ are change in L and θ, respectively, for the event, and ΔD is the buoy displacement. Distances are in m and angles in degrees. Epoch format is DD/MM/YY HH:MM, in UTC. σ_L and σ_θ are the error estimates for L and θ respectively (see text for definition). SI04 and KP08 are in FYI, KP03 and KP04 in MYI.

Baseline (m)	Epoch	S04 (FYI) - K03 (MYI)			S04 (FYI) - K04 (MYI)			S04 (FYI) - K08 (FYI)		
		L (m) σ_L	θ (°) σ_θ	ΔL ΔD Δθ	L (m) σ_L	θ (°) σ_θ	ΔL ΔD Δθ	L (m) σ_L	θ (°) σ_θ	ΔL ΔD Δθ
D13 (Start)	13/12/12 17:00	165.0 4	325.9 1.4	---	211.8 4	327.2 1.1	---	111.5 4	301.8 2.1	---
D13 (End)	14/12/12 09:00	168.3 4	306.1 1.4	3.3 57.4 -19.8	234.6 4	309.4 1.0	22.8 72.6 -17.8	165.7 4	298.8 1.4	54.2 54.7 -3.0

D16 (Start)	16/12/12 20:00	168.4 4	304.6 1.4	---	237.7 4	309.2 1.0	---	164.5 4	295.1 1.4	---
D16 (End)	17/12/12 09:00	180.0 4	319.6 1.3	11.6 42.6 15	246.1 4	324.1 1.0	8.4 62.5 14.9	175.1 4	317.8 1.3	10.6 57.0 22.7

D21 (Start)	21/12/12 18:00	179.3 4	320.8 1.3	---	248.7 4	319.2 1.8	---	169.7 4	312.5 1.4	---
D21 (End)	22/12/12 09:00	84.8 4	298.5 2.7	-94.5 105.4 -22.3	106.7 4	295.6 2.2	-142.0 160.6 -23.6	67.3 4	246.9 3.4	-102.4 165.8 65.6

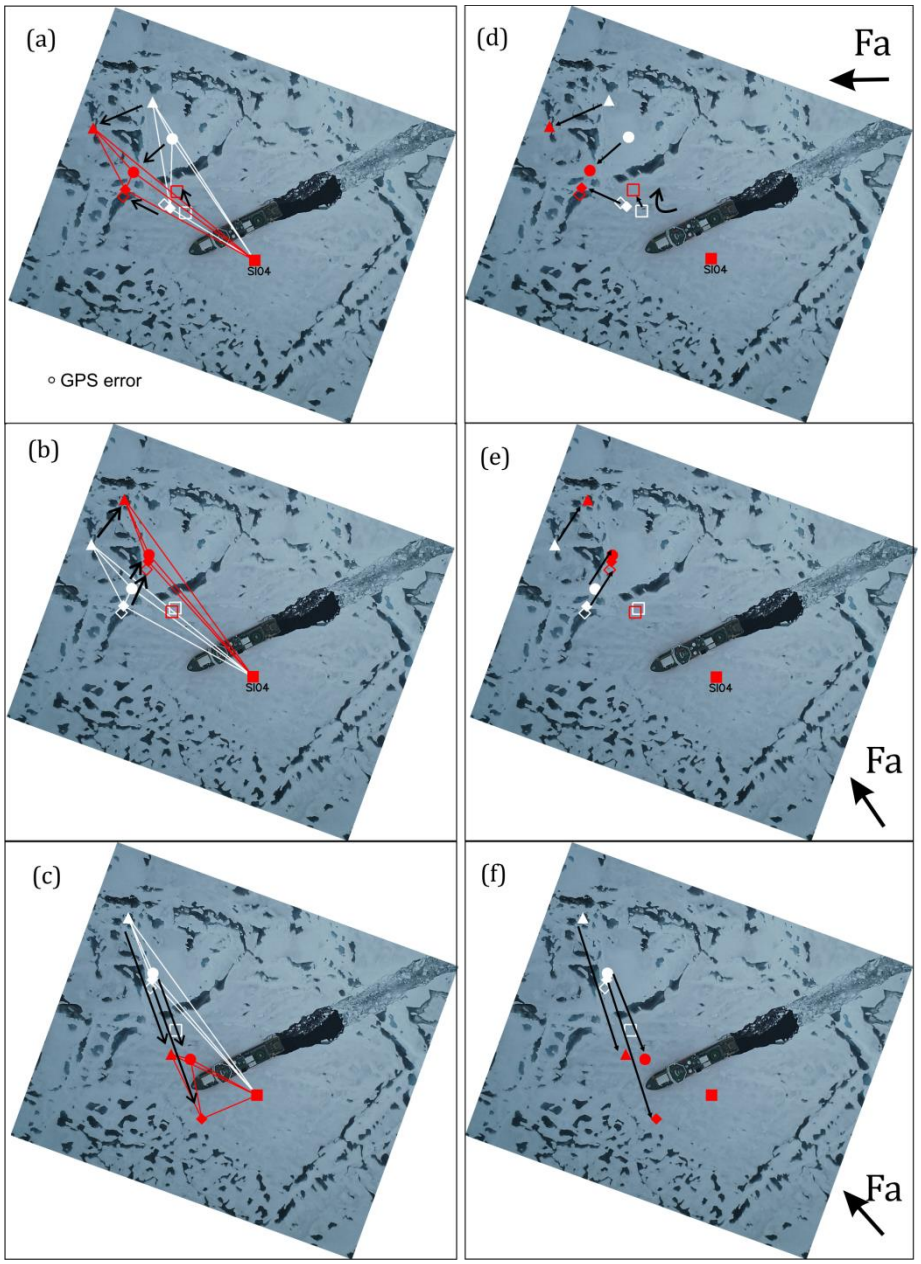

Figure.13 Deformation of buoy arrays during the (a)&(d) D13 event, (b)&(e) D16 event, and (c)&(f) D21 event. In the left panels, the white and red lines represent the buoy arrays before and after the events, respectively. In all panels, black solid arrows show displacement relative to SI04. Closed square, circle, triangle, and diamond symbols mark the locations of SI04, KP03, KP04, and KP08 respectively, and open square and diamond symbols that of SI04 and 2010I respectively. F_a is the direction of wind stress. The aerial photography and buoy arrays of August 14 (Figure 1) here rotated for the floe orientation on December 13. Black circle in (a) is the IMB GPS error estimate (4 m), drawn to scale.

4. Discussions and Conclusions

4.1. Analysis of 2011 SIMBA data

Analysis of 2011 SIMBA data showed that heterogeneous local solar heating effects were sufficiently large enough to cause the observed different melt rates even within an area of ~90 km (a model sub-grid scale). Perovich and others (2008) showed that by the end of August 2007 the ocean had absorbed about 600 MJ m^{-2} of solar energy, which was significantly more than the about 225 MJ m^{-2} required for the observed ice melt. Our observations show that by the end of August the solar heating of the ocean was comparable to the energy required for the observed ice melt. The results generally agree with the model results of Steele and others (2010), in which solar heating was found to contribute a significant portion (ca. 60%) of sea ice melt whilst the dynamic components (advection and diffusive flux) account for the remaining portion.

We have shown here that divergent MY ice experienced significantly different bottom sea ice melt rates at relatively short separations (less than 90 km) over the Chukchi Borderland in August 2011. The ocean-to-ice heat flux calculated along the buoy trajectories showed good agreement with observations and also showed similar differences in heat fluxes. The effects of local solar heating on the differential melt rates were investigated by comparing cumulative solar heat inputs with the heat required for the observed melt rates. This comparison showed that the required heat compared well with the estimated solar heat input to the ocean, and that both quantities were significantly different between the two buoy sites. This can be seen to be the consequence of the drift of one buoy into a more “solar-heated” area in the south, while the other stayed in less “solar-heated” area in the north. Importantly, these large differences in solar heat input and melt rates occurred over a relatively short distance (about 90 km) in the marginal ice zone (MIZ). The effects of dynamic component have not been accounted for in this analysis. Combined analysis of both model and buoy data may permit evaluation the effects of both solar and dynamic effects on sea ice melt in the future. Nonetheless the results suggests that spatial and temporal heterogeneity in local solar heating effects on sea ice melt should be taken into account if one accurately estimate regional scale sea ice mass balance in the MIZ.

4.2. Analysis of 2012 SIMBA data

Our observation during 2012 showed spatial and temporal variations in upper-ocean mixed layer temperature, and ice temperature and phase (i.e. temperature difference after the heating). We first identified four warm water events that were associated with inertial motion of the ice floe. While the third warm water event is likely associated with persistent warm water mass due to solar warming through less ice cover in that region, other three events did not show any particular persistent open water area to be associated with. What is apparent is that the occurrence of warm water mass is clearly associated with inertial motion, but at the same time not all inertial ice motion cause the occurrence of warm water mass. Therefore it is not conclusive that how inertial ice motion is correlated with warm water mass and where warm water mass is originated from. Our observations (and short-term ice moored CTD

observations) indicate the presence of warm water mass within the upper mixed layer during summer month. The origin and effects of such intermittent warm water masses on ice melt is still unknown.

Under free ice drift the effects of acceleration and de-acceleration due to inertial motion were imprinted in the TD values, which caused to higher TD values when ice floe become stagnant. This feature helps to detect the ice bottom during free ice drift condition. However, when ice undergoes autumn freeze-up, the distinction between ice bottom and underlying water becomes less obvious.

2012 SIMBA data also recorded unique small-scale floe deformation events. Previously drifter-based deformation studies were focused in the spatial scale of 10 km or larger (e.g. Hutchings et al. 2011). Using an array of GPS drifters, they found sea ice deformation to follow a multifractal behaviour as reported by Marsan et al (2004). However, when they examined the spectral properties of deformation (which represents the full scaling behaviour, as opposed to Marsan et al. (2004), who considered the scaling properties of the of sea-ice deformation), they found the degree of whitening (flattening) of the spectra increased as the spatial scale decreased, with no apparent universal scaling law for ice deformation that could be applied between 10-70 km. This implies that the largest energy dissipation occurs at the smallest spatial scales (e.g., say km scale, or less), as well as decoupling from large-scale atmospheric wind forcings. This view is supported by Herman and Glowacki (2012), Geiger et al. (2000), and Walter and Overland (1993). The conflicting views on the scaling of deformation at the smallest spatial scales remains unresolved, largely for lack of measurements of transient and higher-stress episodes (e.g., Richter-Menge and Elder, 1998; Richter-Menge et al., 2002), although the existence of the correlation between large-scale forcing and deformation is important question in parameterising deformations in climate models.

Our SIMBA data recorded deformation of the single ice floe at the scale of couple of hundred meters for the first time, and the analysis was made to help to further understand the nature of small-scale deformation and its relation to large-scale wind stress. The results showed the deformation events caused to shrink the baseline distance by almost 50%. This dramatic deformation cannot be explained simply by large-scale wind stress, as strong wind stress during mid-November failed to cause the deformation of the single ice floe but rather freed the ice floe from surrounding (thinner) newly formed ice. As air temperature drop below 10 °C after mid-November, the stiffness of newly formed ice surrounding the ice floe increases as it grows thicker, and thus increases internal ice stress gradient under strong wind stress. Simple force balance analyses of using ice drift and wind data revealed that the dramatic deformation actually occurred by acceleration of the floe following a series of ice fracture events due to increased ice internal stress gradient. In other words our analysis shows the importance of large-scale wind stress, but the propagation of wind stress also depends on internal ice stress (e.g. stiffness of ice) and previous fractures. Therefore our results suggest that simple correlation between deformation and large-scale wind stress is difficult to be observed.

4.3. Concluding remarks

Deployment and analysis of SIMBA data, collaborative between ACCESS, KOPRI and SATICE, revealed i) the effects of local-scale (less than 100 km) variation in solar radiative warming on bottom ice melt, ii) the *potential* effects of inertial ice motion on upper ocean temperature variation as well as effects on the detection of ice bottom from SIMBA data, and iii) further implication of studying floe deformation in conjunction with high-precision GPS buoy (i.e. SATICE). It should be noted that such small-scale variation and events are all operating at a sub-grid scale of current climate models. The study of such sub-grid processes is important if one wants to formulate and improve model parameterisations. For example, our analysis invokes questions like; how important are differential ice bottom melt rate at the sub-grid scale as compared to single value melt rate used within the model grid? Our analysis shows ice bottom melt rate can be more than double or triple within the sub-grid scale. The effects of such sub-grid variability are still unknown and need to be examined further. The same question goes to the effects of inertial ice motion and small-scale deformation we observed in this report.

Interaction with Access partners and external projects

Access partners

We closely worked with OSI SAF, providing SIMBA GPS data for the validation of sea ice drift products produced in OSI SAF.

External projects

Two major collaborations with external partners are with KOrea Polar Research Institute (KOPRI) and SATICE (a European Science Foundation (ESF) PolarCLIMATE project). KOPRI project, Korea-Polar Ocean in Rapid Transition (KOPRI, PM12020) funded by the Ministry of Oceans and Fisheries, Korea, provided in-kind logistical support and berths on board R/V *Araon* for the SIMBA and other collaborative buoy deployment, as well as funded the purchase of six SIMBAs used in this report.

Acknowledgements:

This work was supported by the ACCESS programme, a European Project supported within the Ocean of Tomorrow call. We acknowledge that six SIMBAs were funded by 'Korea-Polar Ocean in Rapid Transition (KOPRI, PM12020)', a project of the Ministry of Oceans and Fisheries, Korea. It is also grateful that KOPRI provides in-kind logistical support to deploy SIMBA buoys, and grateful to KOPRI R/V Araon captain and crews for their supports. High-precision GPS buoy (SATICE) data were used in this report was provided by P. Elosegui at ICE/CSIC, Spain. SATICE programme is a European Science Foundation (ESF) PolarCLIMATE project. The TerraSAR-X SAR imagery usesd in this project was acquired via DLR TSX SSS project to BJH (OCE_0644 and OCE1107). NCEP2 and ECMWF ERA-Interim data used in this report have been obtained from the NCEP2 and the ECMWF data servers respectively. SIMB data is publicly available thanks to CRREL.

References:

Cavalieri, D., T. Markus, and J. Comiso. 2004. updated daily. AMSR-E/Aqua Daily L3 12.5 km Brightness Temperature, Sea Ice Concentration, & Snow Depth Polar Grids V002, 2011. Boulder, Colorado USA: National Snow and Ice Data Center. Digital media.

Ehn, J. K., C. J. Mundy, D. G. Barber, H. Hop, A. Rossnagel, and J. Stewart. 2011. Impact of horizontal spreading on light propagation in melt pond covered seasonal sea ice in the Canadian Arctic, *J. Geophys. Res.,* 116, C00G02, doi:10.1029/2010JC006908.

Elosegui, P., Davis, J.L., Oberlander, D., Baena, R., Ekström, G., 2006. Accuracy of high-rate GPS for seismology, Geophysical Research Letters 33, L11308, doi:10.1029/2006GL026065.

Fofonoff, N. P., and R. C. Millard Jr. 1983. Algorithms for computation of fundamental properties of seawater, Unesco Tech. Pap., Mar. Sci., 44, 53 pp.

Geiger, C.A., Zhao, Y., Liu A.K., Häkkinen, S., 2000. Large-scale comparison between buoy and SSM/I drift and deformation in the Eurasian Basin during winter 1992–1993. Journal of Geophysical Research 105 (C2), 3357–3368.

Herman, A., Glowacki, O., 2012. Variability of sea ice deformation rates in the Arctic and their relationship with basin-scale wind forcing, The Crysophere 6, 1553-1559.

Hutchings, J., Roberts, A., Geiger, C.A., Richter-Menge, J., 2011. Spatial and temporal characterization of sea-ice deformation. Annals of Glaciology 52 (57), 360-368.

Isleifson, D., Hwang, B., Barber, D.G., Scharien, R.K., Shafai, L., 2010. C-Band Polarimetric Backscattering Signatures of Newly Formed Sea Ice During Fall Freeze-Up. IEEE Transactions on Geoscience and Remote Sensing 48 (8), 3256-3267.

Jackson, K., J. Wilkinson, T. Makysm, D. Meldrum, J. Beckers, C. Haas, and D. Mackenzie, 2013, A Novel and Low-Cost Sea Ice Mass Balance Buoy, J. Atmos. Oceanic Tech., 30, 2676-2688, DOI: 10.1175/JTECH-D-13-00058.1.

Markus, T. and S.T. Dokken. 2002. Evaluation of Late Summer Passive Microwave Arctic Sea Ice Retrievals*, IEEE Trans. Geos. Rem. Sens., 40(2),* 348-356.

Marsan. D., Stern, H., Lindsay, R., Weiss J., 2004, Scale Dependence and Localization of the Deformation of Arctic Sea Ice. Physical Review Letters 93 (17), doi:10.1103/PhysRevLett.93.178501.

McPhee, M. G., and J. D. Smith. 1976. Measurements of the turbulent boundary layer under pack ice, *J. Phys. Oceanogr., 6,* 696-711.

McPhee, M. 1992. Turbulent Heat Flux in the Upper Ocean Under Sea Ice, *J. Geophys. Res.*, *97(C4),* 5365-5379.

McPhee, M. G., T. Kikuchi, J. H. Morison, T.P. Stanton. 2003. Ocean-to-ice heat flux at the North Pole environmental observatory, *Geophys. Res. Lett., 30*(24), 2274, doi:10.1029/2003GL018580.

McPhee, M. 2008. Air-Ice-Ocean Interaction: Turbulent Ocean Boundary Layer Exchange Processes, ISBN 978-0-387-78334-5, 215 pp., Springer.

Perovich, D. K., J. A. Richter-Menge, K. F. Jones, and B. Light. 2008. Sunlight, water, and ice: Extreme Arctic sea ice melt during the summer of 2007, *Geophys. Res. Lett., 35,* L11501, doi:10.1029/2008GL034007.

Richter-Menge, J.A., Elder, B.C., 1998. Characteristics of pack ice stress in the Alaskan Beaufort Sea. Journal of Geophysical Research 103 (C10), 21,817–21,829.

Richter-Menge, J.A., McNutt, S. L., Overland, J. E., Kwok, R., 2002. Relating arctic pack ice stress and deformation under winter conditions. Journal of Geophysical Research 107 (C10), 8040, doi:10.1029/2000JC000477.

Steele, M., J. Zhang, and W. Ermold. 2010. Mechanisms of summertime upper Arctic Ocean warming and the effect on sea ice melt, *J. Geophys. Res., 115,* C11004, doi:10.1029/2009JC005849.

Timmermans, M.-L., A. Proshutinsky, R. A. Krishfield, D. K. Perovich, J. A. Richter-Menge, T. P. Stanton, and J. M. Toole. 2011. Surface freshening in the Arctic Ocean's Eurasian Basin: An apparent consequence of recent change in the wind-driven circulation, *J. Geophys. Res., 116,* C00D03, doi:10.1029/2011JC006975.

Uppala, S., D. Dee, S. Kobayashi, P. Berrisford, and A. Simmons. 2008. Towards a climate data assimilation system: Status update of ERA-Interim, *ECMWF Newsletter*, 115, 12-18.

Walter, B.A., Overland, J.E., 1993. The response of lead patterns in the Beaufort Sea to storm-scale wind forcing. Annuals of Glaciology, 17, 219–226.

Zib, B., J., X. Dong, B. Xi, and A. Kennedy. 2012. Evaluation and Intercomparison of Cloud Fraction and Radiative Fluxes in Recent Reanalyses over the Arctic Using BSRN Surface Observations. *J. Climate, 25,* 2291–2305, doi: http://dx.doi.org/10.1175/JCLI-D-11-00147.1.